Deposition Behavior and Microstructural Features of Vacuum Kinetic Sprayed Aluminum Nitride

Hyungkwon Park, Jeeae Heo, Fei Cao, Juhyuk Kwon, Kicheol Kang, Gyuyeol Bae, and Changhee Lee

The vacuum kinetic spray (VKS) method is a relatively advanced technology by which thin and dense ceramic coatings can be fabricated via the high-speed impact of submicron-sized particles at room temperature. However, the actual bonding mechanism associated with the VKS process has not yet been elucidated. In this study, AlN powders were pretreated through ball-milling and heat-treatment processes in order to investigate the effects of microstructural changes on the deposition behavior. It was found that ball-milled and heat-treated powder with polycrystals formed by partially aligned dislocations showed considerably higher deposition rates when compared to only ball-milled powder with tangled dislocations. Therefore, in the VKS process, the deposition behavior is shown to be affected by not only the particle size and defect density, but also the microstructure of the feedstock powder.

1. Introduction

The fabrication of ceramics usually requires a high temperature process due to the high melting point of the materials. Such a requirement increases the manufacturing costs and limits the shape of the products. In addition, oxidation or damage resulting from a high temperature treatment degrades the quality of the finished product. These problems seriously hinder the application of ceramic materials in various industries, specifically in fields that require miniaturization of devices such as electro-ceramic components, optical components, semiconductors, and microelectromechanical systems (Ref 1, 2). Furthermore,

in conventional techniques such as sputtering (Ref 3), metalorganic chemical vapor deposition (Ref 4), ion beam enhanced deposition (Ref 5), or sol-gel processing (Ref 6), the deposition rate is comparatively slow and some stresses are caused during processing, which makes the fabrication of ceramic films inefficient.

The vacuum kinetic spray (VKS) technique, also called aerosol deposition method or vacuum cold spray, is a relatively advanced and very attractive technology by which thin or thick ceramic films can be fabricated at high deposition rates and at room temperature. In addition, the formed structure has a very dense coating layer, and the process cost is comparatively low (Ref 7-10). Thus, VKS technology has been researched for the fabrication of various products, including piezoelectric devices (Ref 11-13), dye-sensitized solar cells (Ref 14-16), solid oxide fuel cell (Ref 17-19), and artificial bone (Ref 20, 21). The principle of the VKS process is based on the impact of particles accelerated by a pressure gap between the deposition chamber and the aerosol chamber. In general, submicron-size ceramic powders are used and the resulting coatings have a nanocrystalline structure. It is mainly hypothesized that, in the VKS process, bonding occurs by the fracture or plastic deformation of particles (Ref 7, 9, 22-26). However, detailed bonding mechanisms have not yet been elucidated.

In this study, powders were pretreated through ball-milling and heat-treatment procedures so as to investigate the effects of microstructural features on the deposition behavior during the VKS process. These pretreatments caused changes in the defect density, the formation of dislocations, and the crystallinity for each powder. As a result, different deposition behaviors and several crucial microstructural features were observed, through which fracture aspects induced by the microstructures and the consequential bonding mechanisms were discussed.

Hyungkwon Park, Jeeae Heo, Fei Cao, Juhyuk Kwon, Kicheol Kang, Gyuyeol Bae, and **Changhee Lee,** Kinetic Spray Coating Laboratory (NRL), Division of Materials Science and Engineering, Hanyang University, 17 Haengdang-dong, Seongdong-gu, Seoul 133-791, South Korea. Contact e-mail: chlee@hanyang.ac.kr.

Table 1 Ball-milling process parameters

RPM (rotation per minute)	250
Environment	Ethanol
ZrO_2 ball:powder, wt.%	15:1
Time	5 h

Table 2 Heat-treatment process parameters

Environment	Ar
Temperature	800 °C
Temp change rate	10 °C/min
Time	4 h

2. Experimental Method

2.1 Material Preparation

Aluminum nitride powder (Shineso Co. Ltd., China) with a purity of 99.5% was used as a feedstock material. In order to investigate the effects of microstructure on the deposition behavior in the VKS procedure, ball-milling and heat-treatment processes were conducted (Ref 7, 28, 29). For the ball-milling, the powder was first mixed with zirconia balls of various sizes in a weight ratio of 1:15 and then ball-milled for 5 h at 250 rpm in an ethanol environment (denoted as BM5h). A heat-treatment was also conducted at 800 °C for 4 h in an Ar atmosphere after the ball-milling (denoted as HT5h) (Ref 28, 29). These pretreated powders were dried for several hours and a silica glass substrate with a size of 76×26 mm^2 and 1 mm thickness was cleaned before the coating experiments. The detailed experimental conditions are shown in Tables 1 and 2.

2.2 VKS Coating

AlN coatings were deposited via the VKS process, as schematically shown in previous study (Ref 7); the specific conditions are listed in Table 3. A convergent-barrel type slit nozzle with an orifice of 5.0×0.5 mm^2 was used to accelerate the particles with helium process gas at a pressure of 0.6 MPa and a flow rate of 6 L/min. The standoff distance and gun transverse speed were fixed at 8 mm and 1 mm/s, respectively. The coating process began when the pressure of the deposition chamber was at 6.0×10^{-2} Torr, and the pressure was maintained around 9.8×10^{-2} Torr during the deposition procedure. To examine the deposition rates in each coating case, 1, 5, and 10 spraying passes were performed. The powder feed rates of BM5h and HT5h powders were estimated as about 3.908 and 4.053 mg/s, respectively.

2.3 Characterization of Powder and Coating Microstructure

The powder morphology, coating surface, and cross-section of the samples were observed using a field emission scanning electron microscope (FE-SEM, JSM-6330F, Japan), while the particle size and coating thickness were

Table 3 VKS coating parameters

Nozzle type	Slit nozzle
Carrier gas	He
Gas pressure	0.6 MPa
Consumption of carrier gas	6 L/min
Standoff distance	8 mm
Pressure in deposition chamber	9.8×10^{-2} Torr
Pass number	1, 5, 10
Gun traverse speed	1 mm/s

estimated with Image-Pro Plus software. The phase of the powder was examined using x-ray diffractometry (XRD, D/MAX-2500, Rigaku, Japan). The specimens used in imaging the coating cross-section were prepared by focused ion beam (FIB, FB-2100, Hitachi, Japan) techniques, and the microstructure of the powders and coatings were investigated using a high resolution transmission electron microscope (HR-TEM, Tecnai G^2 F30 S-Twin, Netherlands) operated at 300 kV. To examine the crystallinity of the microstructure, selected area electron diffraction (SAED) and fast Fourier transformation (FFT) patterns were acquired and analyzed using appropriate software (DigitalMicrograph, Gatan).

3. Results and Discussion

3.1 Characteristics of Each Powder

The morphology of each powder is shown in Fig. 1. The as-received powder (denoted as AR) had a size of around 6.41 μm and a hard agglomerated shape consisting of micron-sized primary particles (Fig. 1a). However, as confirmed in Fig. 1(b), the particles were fractured during the ball-milling and thus, the particle shape became relatively irregular and faceted. Moreover, the powder size decreased significantly from a mean size of 6.41-0.68 μm with a decrease in the size range, as confirmed in Fig. 2(a). After the heat-treatment, the powder morphology was similar to the case of BM5h, and the size did not change considerably (0.76 μm), as shown in Fig. 1(c) and 2(a). Thus, it was expected that the BM5h and HT5h powders were more appropriate for use as a coating when compared to the as-received powder because the particle size is a very important factor for successful deposition in a VKS system (Ref 7, 9).

To investigate the effect of structure on the deposition behavior, the phase of each powder was examined by XRD; the results are shown in Fig. 2(b). The findings revealed that the initial wurtzite structure of the powders was preserved even after the powder pretreatment.

To distinguish between the microstructural features of BM5h and HT5h, each powder was examined using HR-TEM. A TEM micrograph of a BM5h particle with its SAED pattern is shown in Fig. 3(a). The pattern indicates the existence of a single crystal, a result that was confirmed with HREM images of the particle, as shown in Fig. 3(b). The areas A and B in Fig. 3(b) show not only the same lattice orientation, but the FFT pattern, which
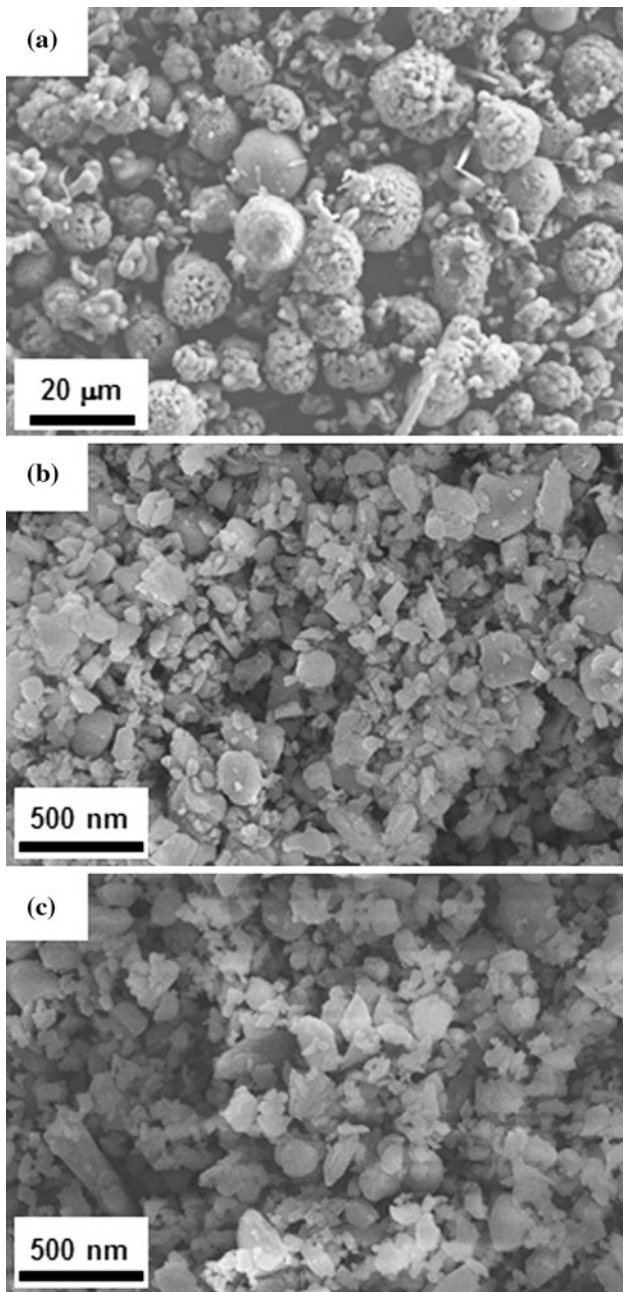
Fig. 1 FE-SEM micrographs of AlN powder: (a) as-received, (b) ball-milled for 5 h, and (c) ball-milled for 5 h and heat-treated at 800 °C for 4 h

indicated that the particle consisted of a single crystal or had a coarse grain.

In contrast to the BM5h powder, the SAED pattern of HT5h showed a ring pattern representative of a polycrystal, as shown in Fig. 4(a). In addition, three grains were observed with different lattice orientations, and FFT patterns in Fig. 4(b), although the figure was a very small part of Fig. 4(a). Thus, it was considered that the heat-treatment affected the microstructural features of the samples. Figure 5 illustrates the changes caused by the

pretreatment, including the formation and evolution of defects: (a) as-received powder has only a few defects; (b) during the ball-milling, the powder is fractured and many defects are generated in a tangle formation due to severe ball impacts (Ref 25, 27); (c) the defect density then decreases by recovery and dislocations are partially aligned, resulting in the formation of subgrains during heat-treatment; (d) perfect subgrains are formed by sub-grain boundaries where dislocations are aligned. At this point, the recovery phenomenon is terminated. Although the melting temperature, 2200 °C, and recrystallization temperature (Ref 30) are significantly higher than the heat-treatment condition, 800 °C, it was thought that the high internal energy state induced by ball impacts served to lower the recovery temperature. As a result, imperfect subgrains were formed, resulting in a ring-shaped SAED pattern that indicates the presence of a polycrystal.

3.2 Deposition Behavior

The deposition behaviors of different pretreated powders are shown in Fig. 6; the abscissa and ordinate axes signify the number of passes and the coating thickness, respectively. As mentioned above, the as-received powder was not appropriate for VKS coating because it was too coarse to transform into an aerosol state (6.41 μm) and not enough defects were present for fragmentations upon impact. Thus, it was considered that a sufficient amount of new surfaces, which was thought to be a thermodynamically unstable state, was not created. As a result, a film was not formed even though up to ten passes were carried out in the coating process. However, when the BM5h powder was used, coatings with thicknesses of ~2-7 μm were successfully deposited, as confirmed in Fig. 7(a). Such a result may be attributed to the fact that the powder had a proper size range in which a relatively large amount of particles was able to become an aerosol state, compared to the case of AR, and thus, take part in the deposition. In addition, when compared to the as-received powder, the numerous defects generated in BM5h by ball-milling allowed the particles to be fragmented, whereby new and unstable surfaces were easily created. In the case of HT5h, the deposition thicknesses were dramatically increased to ~12-25 μm, as shown in Fig. 7(b). Considering the notion that defects make fragmentation occur more easily, this thickness trend seems to come not from the defect density, but microstructural differences between BM5h and HT5h.

When BM5h powder was used, the deposition tendency was in agreement with that general observed for VKS coatings, i.e., the coating thickness increased with the spraying pass number. However, in the case of HT5h, the film thickness increased steadily up to five passes, but then fell. Such a phenomenon is not clearly understood and more experiments are needed to investigate this deposition behavior.

3.3 Microstructural Features of Each Coating

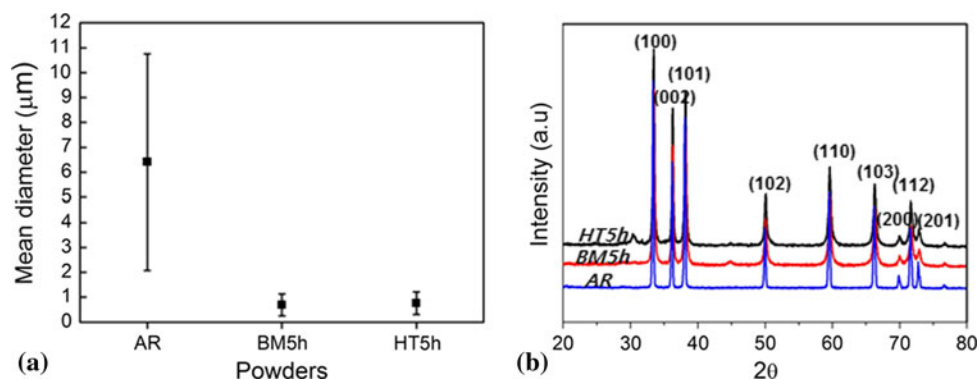SEM images showing the surface morphology of each coating made with BM5h powders (denoted as BM5h

Fig. 2 (a) Powder size distribution and (b) XRD patterns of as-received and pretreated powders
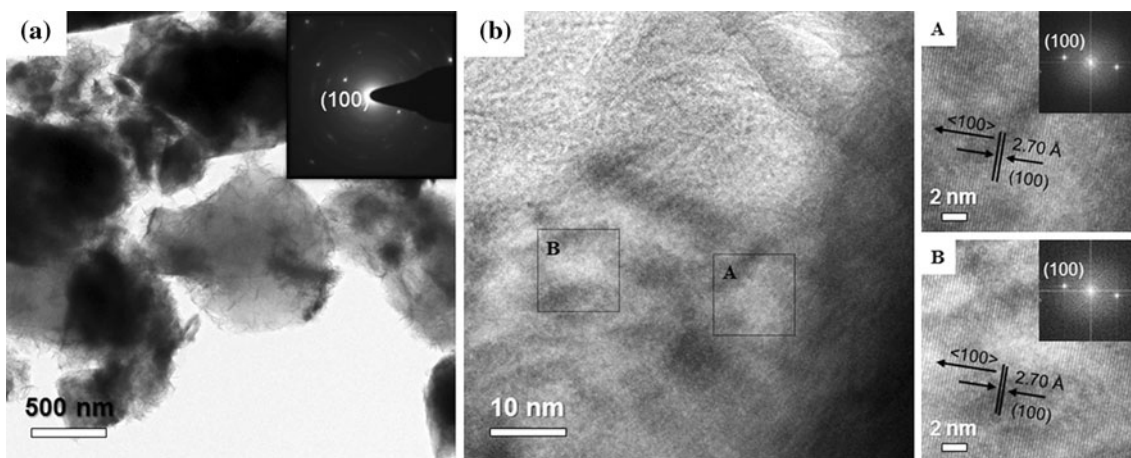

Fig. 3 (a) TEM micrographs of a powder ball-milled for 5 h (inset is a SAED pattern), and (b) HR-TEM image of a particle with FFT patterns
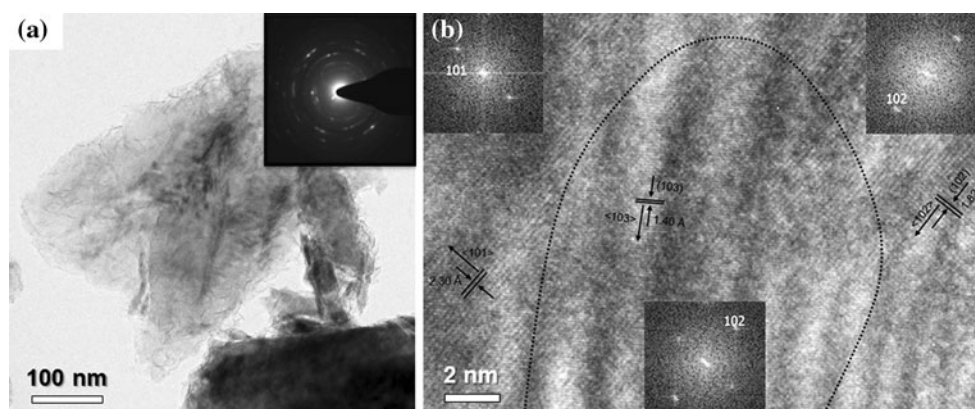

Fig. 4 (a) TEM micrographs of a ball-milled and heat-treated powder (inset is a SAED pattern), and (b) HR-TEM image of a particle (insets are FFT patterns)

coating) and HT5h powders (denoted as HT5h coating) are displayed in Fig. 8(a), (c) and 8(b), (d), respectively. The dashed-boxed regions in Fig. 8(a) and (b) were magnified and are shown in Fig. 8(c) and (d), respectively. The surface of the HT5h coating was relatively rough when compared to that of the BM5h coating, as illustrated

in Fig. 8(a) and (b). In the high-magnification micrograph, a tamped-shape surface was observed for the BM5h coating (Fig. 8c), whereas several nano-sized fragments were observed at the surface of the HT5h coating (Fig. 8d). Such fragments caused the surface of the HT5h coating to be rough, and it is inferred that the HT5h
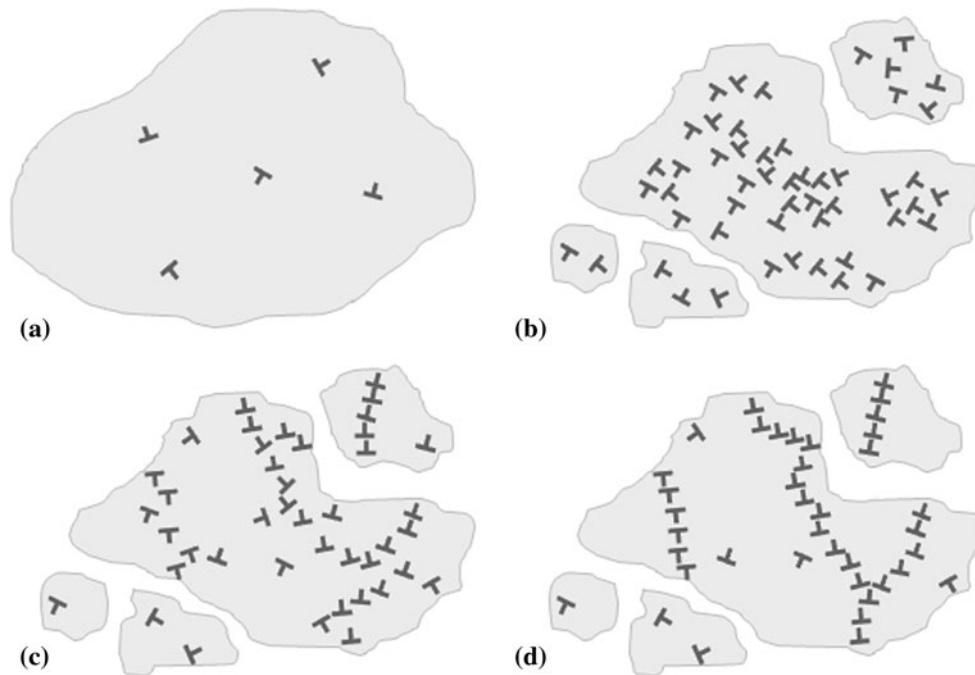
Fig. 5 Schematic illustration of defect formation in (a) as-received, (b) ball-milled, (c) imperfectly recovered, and (d) completely recovered particles
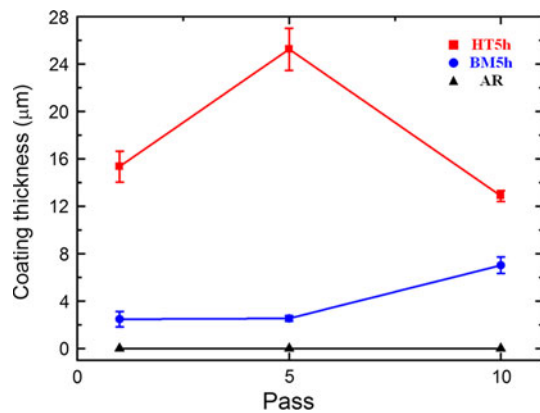

Fig. 6 Deposition behaviors of different pretreated powders

particles were more severely fragmented. On the other hand, it is thought that the tamped-shape surface observed in the case of the BM5h coating came from the fact that the particles were not sufficiently fractured, which induced a tamping effect on the surface (Ref 10, 23, 24). Thus, large-size fragments were observed in Fig. 8(c).

TEM cross-sectional micrographs of each coating are shown in Fig. 9. Each coating showed a polycrystalline SAED pattern; such patterns are often associated with VKS coatings. A distinct difference between BM5h in Fig. 9(a) and HT5h in Fig. 9(b) was the fraction of dark and bright contrast. Thus, the cross-section of each coating was examined in high-magnification TEM mode so as to focus on each contrast region.

The dark contrast region of the BM5h cross-section is shown in Fig. 10(a). The dashed-boxed region in Fig. 10(a) was magnified and is displayed in Fig. 10(b). It was confirmed that the dark contrast region was comprised of several nano-sized grains with random orientations. In contrast, very coarse grains were observed in the bright contrast region, as shown in Fig. 10(c) and confirmed in Fig. 10(d) and (e). That is, the lattice orientation, and FFT pattern in Fig. 10(d) and (e), denoted by the right and left dashed-boxed regions in Fig. 10(c), were almost identical, although the lattice and pattern were shifted slightly by defects or nano-sized cracks. As a result, in the case of the BM5h coating, the contrast difference in the TEM micrographs was generated by the formation of grains with various orientations.

The cross-section of the HT5h coating is displayed in Fig. 11(a). As mentioned above, the dark contrast region of the BM5h coating consisted of nano-sized grains with random orientations. Similarly, the dark contrast region of the HT5h coating was also composed of nano-sized grains with irregular orientations, as shown in Fig. 11(b), which is a high-magnification image of the dashed-boxed region in Fig. 11(a). However, in the case of the HT5h coating, a relatively higher dark contrast fraction was observed, as illustrated in Fig. 9(b). In other words, a larger fraction of nano-grains was formed in the HT5h coating and thus, it is inferred that the HT5h particles fragmented more severely. In the bright contrast region of the HT5h coating, the region in which the crystallinity was comparatively well-preserved was found, as shown in Fig. 11(c) and confirmed from the FFT pattern displayed in Fig. 11(d).
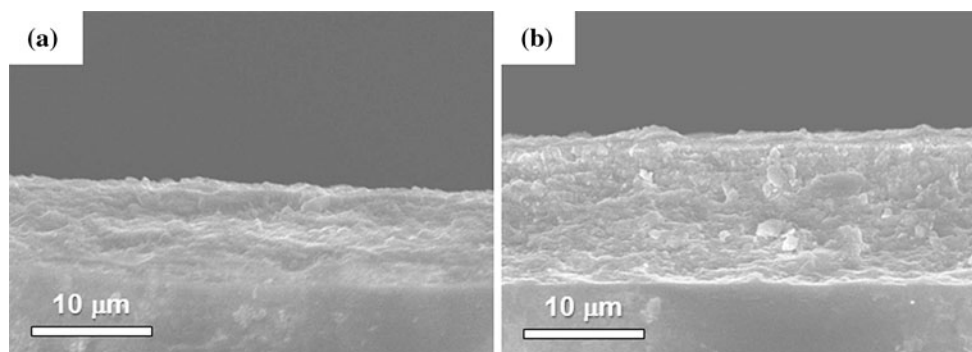
Fig. 7 Cross-sectional SEM micrographs of coatings formed using (a) only ball-milled powders and (b) ball-milled and heat-treated powders
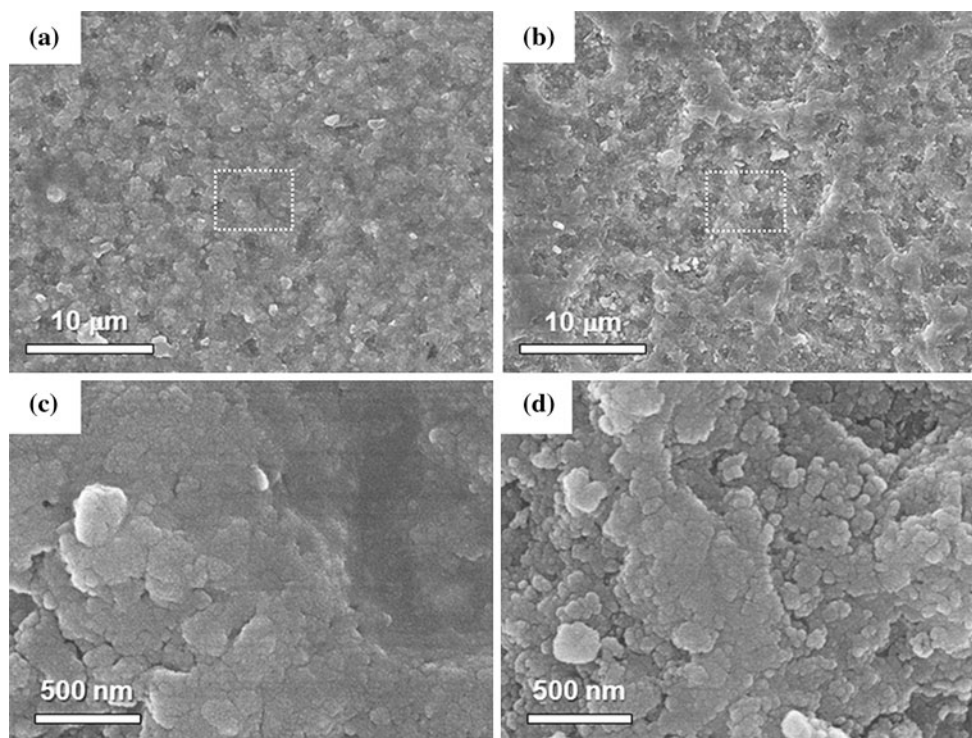

Fig. 8 Surface morphology of coatings using (a) only ball-milled powders, and (b) ball-milled and heat-treated powders, and (c), (d) higher magnification image of the dashed-boxed region in (a) and (b)

Based on the above findings, it is believed that the HT5h particles are fragmented more efficiently and severely, which in turn allows for a more effective deposition. Because the main difference between the BM5h and HT5h particles was the crystallinity, it is rational to assume that the distinct deposition difference of the two different particles come from this crystallinity difference. When each particle impacts the substrate, cracking takes place and the cracks dissipate their energy for propagation because of the resistance resulting from the new surfaces that are created. In the case of BM5h, the particle was single crystal and, defects were irregularly formed and tangled, as illustrated in Fig. 5(b). Thus, this type of defect formation is not effective for crack propagation, and the cracks must consume a great deal of their energy across the grains, leading to transgranular cracking. In addition, the crack propagation behavior, like hardening, can be disturbed by defect formation. As a result, in the BM5h coating, large fragments on the coating surface and a tamped-shape surface were observed due to incomplete fracture, as shown in Fig. 8(c). Thus, coarse grains were also observed in the coating layer, as illustrated in Fig. 10(c).

In contrast to BM5h, dislocations were reduced and partially aligned in HT5h, as depicted in Fig. 6(c). From previous research (Ref 31), it is known that crack behavior is affected by the grain size, especially as the size reaches under several microns. Schematic images of the crack propagation mode induced by the grain size are shown in Fig. 12. The fracture mode for ceramics with relatively
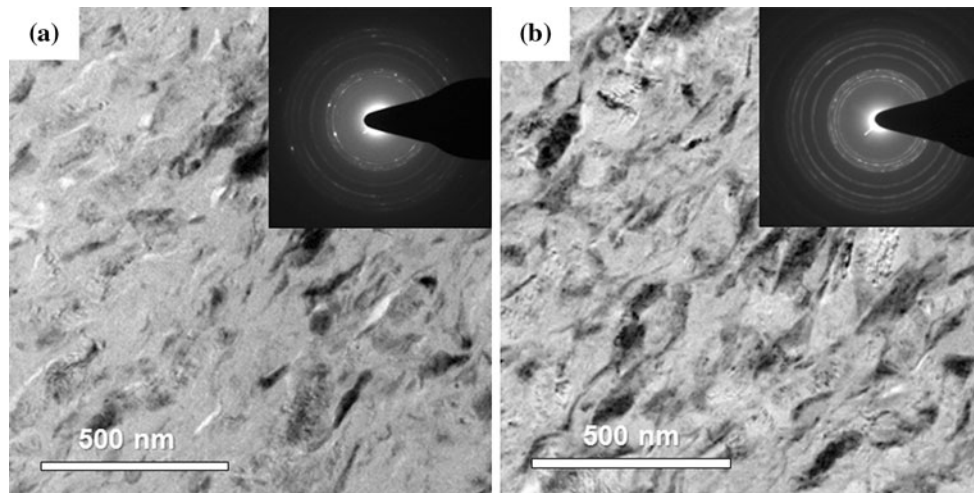
Fig. 9 TEM micrographs of coating cross-sections for (a) ball-milled powders and (b) ball-milled and heat-treated powders
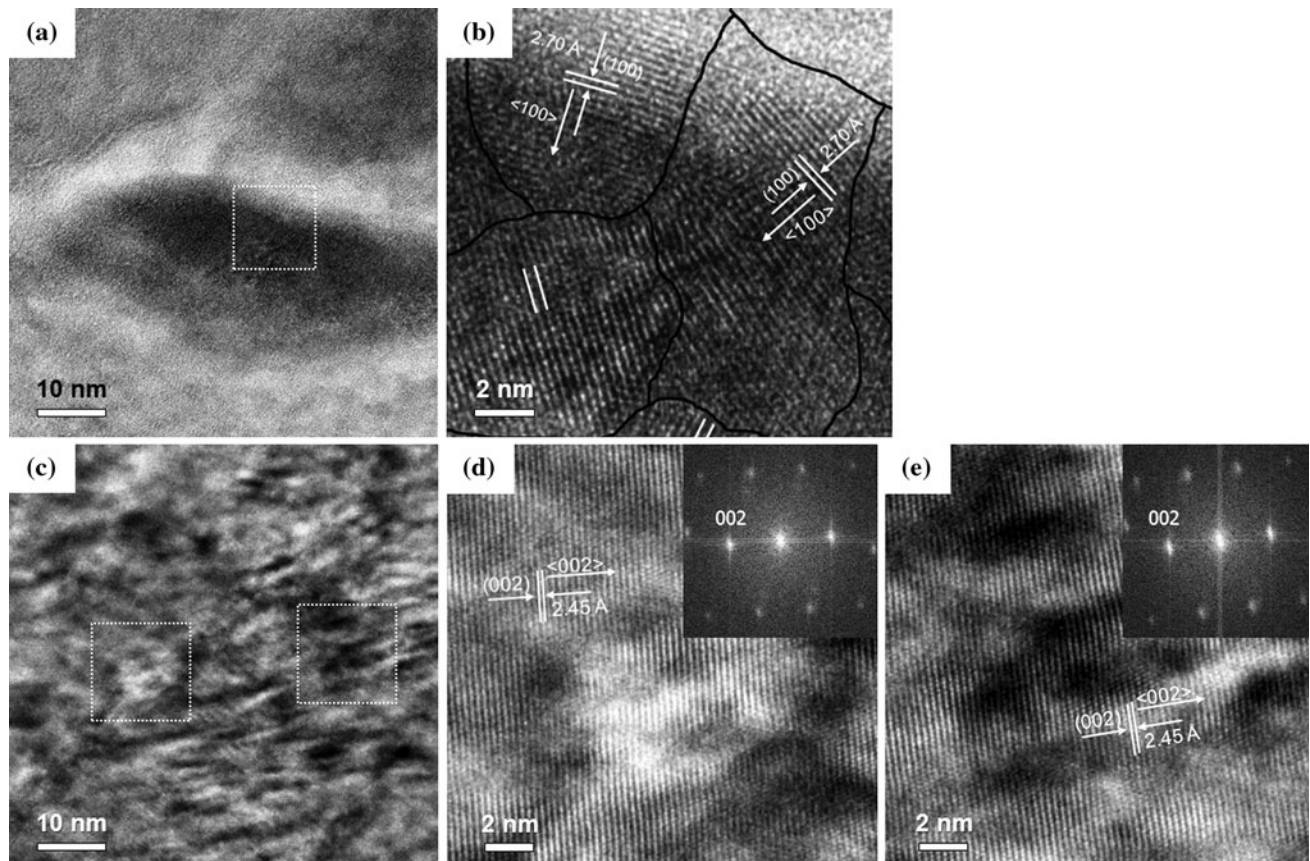

Fig. 10 HR-TEM cross-sectional micrographs of a coating made with powder ball-milled for 5 h: (a) dark contrast region, (b) higher magnification image of the dashed boxed region in (a), (c) bright contrast region, and (d), (e) higher magnification images of the left and right dashed-boxed regions in (c)

larger grains is generally transgranular fracture (Fig. 12a), but the mode can be changed to intergranular fracture as the grain size decreases (Fig. 12b). Therefore, it is inferred that, although the subgrains of the HT5h particles are not perfect, dislocation alignment played a significant role in

the direction of the crack propagation (Ref 32, 33). Consequently, the particles were able to be shattered more easily than the case of BM5h, which was observed as the shape of a higher fraction of the nano-sized grain and the dark contrast region in the HT5h coating layer in
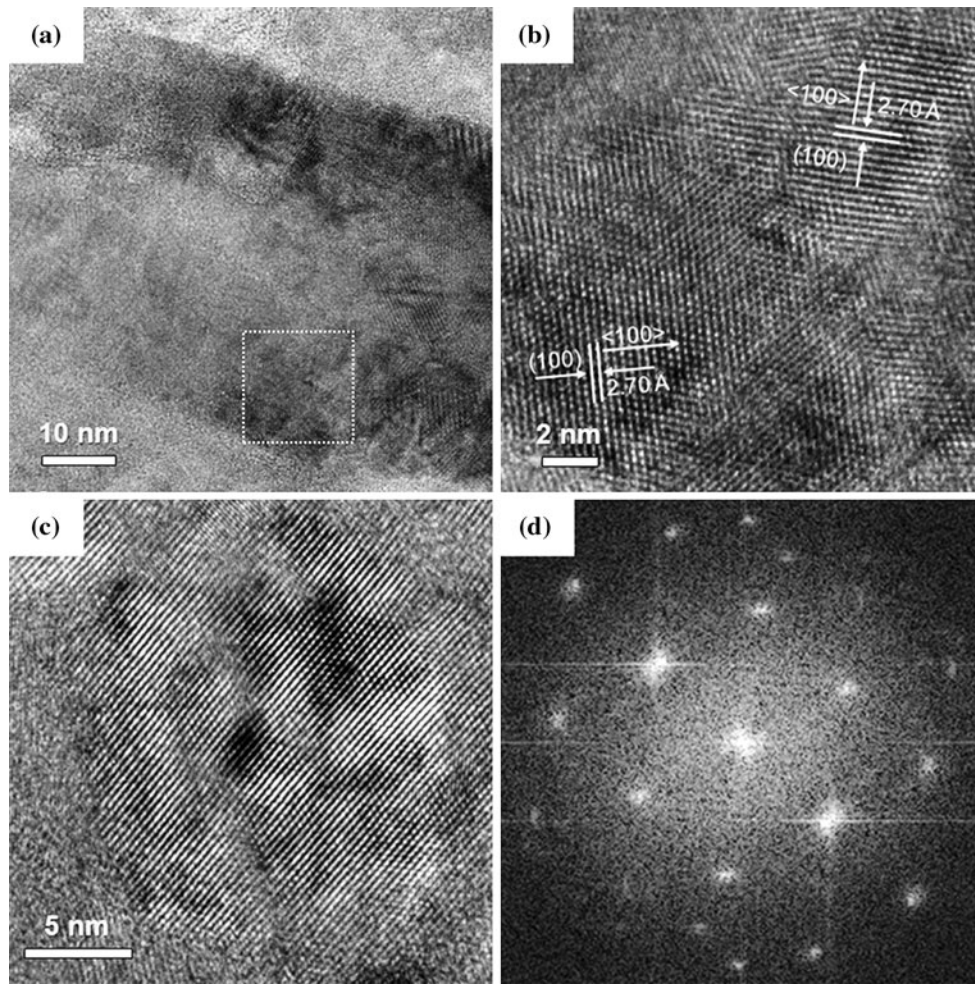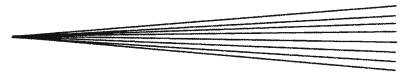
Fig. 11 (a) HR-TEM cross-sectional images of ball-milled and heat-treated powder coatings: (a) dark contrast region, (b) higher magnification image of the dashed boxed region in (a), (c) single grain region, and (d) the FFT pattern of the single grain
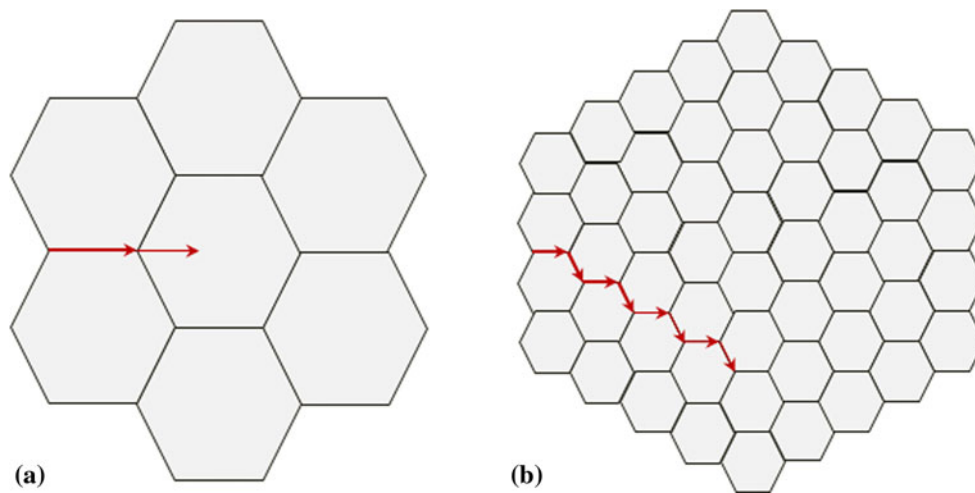

Fig. 12 Schematic illustration of the crack propagation path in the case of (a) relatively large grains and (b) fine grains

Fig. 9(b). Furthermore, finer fragments were observed on the surface in Fig. 8(d), and single grains (relatively larger than nano-grains) which were previously subgrains existed in the coating, as illustrated in Fig. 11(c) and (d).

4. Conclusion

In this study, three types of powders, as-received, ball-milled for 5 h (BM5h), and ball-milled for 5 h and heat-treated at 800 °C for 4 h (HT5h), were used to form a coating on a glass substrate in order to investigate the effect of microstructural features on the deposition behavior. The powder particle size decreased and many defects were generated during ball-milling. However, some defects in the powder were recovered, and dislocations were partially aligned, resulting in a polycrystalline structure. The important features of each powder and coating may be summarized as follows:

In the case of BM5h powder, it consisted of single crystals or comparatively large grains. However, after heat-treatment, the density of defects was reduced and dislocations were partially aligned. As a result, polycrystals were formed in HT5h powder by the recovery process. This distinct microstructure difference resulted in the coating deposition rate in VKS system. That is, the HT5h coating was not only obviously thicker but also had a higher fraction of the dark contrast region consisting of smaller nano-size grains than the case of BM5h coating. In addition, it is observed that finer fragments observed on the HT5h coating surface and significant larger grains observed in the BM5h coating layer. Based on these observations, it is inferred that in the case of HT5h, the particles were more efficiently fragmented by the aligned dislocations, which finally resulted in higher deposition rate. Thus, it is concluded that the deposition behavior is affected not only by the particle size and defect density, but also by the microstructure of the feedstock powder in the VKS process.

Acknowledgments

References

1. N. Setter, Electroceramics: Looking Ahead, *J. Eur. Ceram. Soc.*, 2001, **21**, p 1279-1293
2. Q.F. Zhou, H.L.W. Chan, and C.L. Choy, PZT Ceramic/Ceramic 0-3 Nanocomposite Films for Ultrasonic Transducer Applications, *Thin Solid Films*, 2000, **375**, p 95-99
3. T. Haccart, E. Cattan, and D. Remiens, Dielectric, Ferroelectric and Piezoelectric Properties of Sputtered PZT Thin Films on Si Substrates: Influence of Film Thickness and Orientation, *Semicond. Phys. Quantum Electron.*, 2002, **5**(1), p 78-88
4. Y. Sakashita, T. Ono, and H. Segawa, Preparation and Electrical Properties of MOCVD Deposited PZT Thin Films, *J. Appl. Phys.*, 1991, **69**(12), p 8352-8357
5. Z. An, C. Men, Z. Xu, P.K. Chu, and C. Lin, Electrical Properties of AlN Thin Films Prepared by Ion Beam Enhanced Deposition, *Surf. Coat. Technol.*, 2005, **196**, p 130-134
6. M. Jain, S.B. Majumder, R. Guo, A.S. Bhalla, and R.S. Katiyar, Synthesis and Characterization of Lead Strontium Titanate Thin Films by Sol-Gel Technique, *Mater. Lett.*, 2002, **56**, p 692-697
7. J. Akedo, Room Temperature Impact Consolidation (RTIC) of Fine Ceramic Powder by Aerosol Deposition Method and Applications to Microdevices, *J. Therm. Spray. Technol.*, 2008, **17**(2), p 181-198
8. S. Nam, N. Mori, H. Kakemoto, S. Wada, J. Akedo, and T. Tsurumi, Alumina Thick Films as Integral Substrates Using Aerosol Deposition Method, *Jpn. J. Appl. Phys.*, 2004, **43**(8A), p 5414-5418
9. J. Akedo, Aerosol Deposition of Ceramic Thick Films at Room Temperature: Densification Mechanism of Ceramic Layers, *J. Am. Ceram. Soc.*, 2006, **89**(6), p 1834-1839
10. Y.-Y. Wang, Y. Liu, G.-J. Yang, J.-J. Feng, and K. Kusumoto, Effect of Microstructure on the Electrical Properties of Nano-Structured TiN Coatings Deposited by Vacuum Cold Spray, *J. Therm. Spray. Technol.*, 2010, **19**(6), p 1231-1237
11. J. Akedo and M. Lebedev, Piezoelectric Properties and Poling Effect of Pb(Zr,Ti)O$_3$ Thick Films Prepared for Microactuators by Aerosol Deposition, *Appl. Phys. Lett.*, 2000, **77**(11), p 1710-1712
12. J. Ryu, J. Choi, B. Hahn, D. Park, W. Yoon, and K. Kim, Fabrication and Ferroelectric Properties of Highly Dense Lead-Free Piezoelectric (K$_{0.5}$Na$_{0.5}$)NbO$_3$ Thick Films by Aerosol Deposition, *Appl. Phys. Lett.*, 2007, **90**(15), p. 152901 (1-3)
13. X.-Y. Wang, C.-Y. Lee, C.-J. Peng, P.-Y. Chen, and P.-Z. Chang, A Micrometer Scale and Low Temperature PZT Thick Film MEMS Process Utilizing an Aerosol Deposition Method, *Sens. Actuators A*, 2008, **143**, p 469-474
14. S.-Q. Fan, G.-J. Yang, C.-J. Li, G.-J. Liu, C.-X. Li, and L.-Z. Zhang, Characterization of Microstructure of Nano-TiO$_2$ Coating Deposited by Vacuum Cold Spraying, *J. Therm. Spray. Technol.*, 2006, **15**(4), p 513-517
15. S.-Q. Fan, C.-J. Li, G.-J. Yang, L.-Z. Zhang, J.-C. Gao, and Y.-X. Xi, Fabrication of Nano-TiO$_2$ Coating for Dye-Sensitized Solar Cell by Vacuum Cold Spraying at Room Temperature, *J. Therm. Spray. Technol.*, 2007, **16**(5-6), p 893-897
16. G.-J. Yang, C.-J. Li, K.-X. Liao, X.-L. He, S. Li, and S.-Q. Fan, Influence of Gas Flow During Vacuum Cold Spraying of Nano-Porous TiO$_2$ Film by Using Strengthened Nanostructured Powder on Performance of Dye-Sensitized Solar Cell, *Thin Solid Films*, 2011, **519**, p 4709-4713
17. J. Choi, J. Lee, D. Park, B. Hahn, W. Yoon, and H. Lin, Oxidation Resistance Coating of LSM and LSCF on SOFC Metallic Interconnects by the Aerosol Deposition Process, *J. Am. Ceram. Soc.*, 2007, **90**(6), p 1926-1929
18. J. Choi, D. Park, B. Seong, and H. Bae, Low-Temperature Preparation of Dense (Gd,Ce)O$_2$-δ-Gd$_2$O$_3$ Composite Buffer Layer by Aerosol Deposition for YSZ Electrolyte-Based SOFC, *Int. J. Hydrogen Energy*, 2012, **37**, p 9809-9815
19. J. Choi, K. Cho, J. Choi, J. Ryu, B. Hahn, J. Kim, C. Ahn, W. Yoon, J. Yun, and D. Park, Effects of Annealing Temperature on Solid Oxide Fuel Cells Containing (La,Sr)(Ga,Mg,Co)O$_3$-δ Electrolyte Prepared by Aerosol Deposition, *Mater. Lett.*, 2012, **17**, p 44-47
20. S. Kim, D. Seo, and J. Lee, Fabrication of Xenogeneic Bone-Derived Hydroxyapatite Thin Film by Aerosol Deposition Method, *Appl. Surf. Sci.*, 2008, **255**, p 388-390
21. B. Hahn, D. Park, J. Choi, J. Ryu, W. Yoon, K. Kim, C. Park, and H. Kim, Dense Nanostructured Hydroxyapatite Coating on Titanium by Aerosol Deposition, *J. Am. Ceram. Soc.*, 2009, **92**(3), p 683-687
22. M. Lebedev, J. Akedo, and T. Ito, Substrate Heating Effects on Hardness of an α-Al$_2$O$_3$ Thick Film Formed by Aerosol Deposition Method, *J. Cryst. Growth*, 2005, **275**, p e1301-e1306
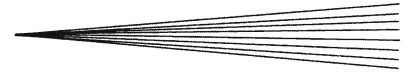
23. D. Chun and S. Ahn, Deposition Mechanism of Dry Sprayed Ceramic Particles at Room Temperature Using a Nano-Particle Deposition System, *Acta Mater.*, 2011, **59**, p 2693-2703

24. D. Lee, H. Kim, Y. Kim, Y. Yun, and S. Nam, Growth Process of α-Al$_2$O$_3$ Ceramic Films on Metal Substrates Fabricated at Room Temperature by Aerosol Deposition, *J. Am. Ceram. Soc.*, 2011, **94**(9), p 3131-3138

25. W. Yong, G. Bae, K. Kang, and C. Lee, The Effect of Fracture-Induced Ceramic Free Surfaces for Vacuum Kinetic Spray Bonding, *International Thermal Spray Conference*, Sept 27-29, 2011 (Hamburg), DVS 276 Deutscher Verband für Schweißen, 2011, p 896-900

26. F. Cao, H. Park, G. Bae, J. Heo, and C. Lee, Microstructure Evolution of Titanium Nitride during Vacuum Kinetic Spraying, *J. Am. Ceram. Soc.*, 2013, **96**(1), p 40-43

27. Z.Q. Yang, L.L. He, and H.Q. Ye, The Effect of Ball Milling on the Microstructure of Ceramic AlN, *Mater. Sci. Eng A*, 2002, **A323**, p 354-357

28. A. Iwata, J. Akedo, and M. Lebedev, Cubic Aluminum Nitride Transformed Under Reduced Pressure Using Aerosol Deposition Method, *J. Am. Ceran. Soc.*, 2005, **88**(4), p 1067-1069

29. A. Iwata and J. Akedo, Hexagonal to Cubic Crystal Structure Transformation During Aerosol Deposition of Aluminum Nitride, *J. Cryst. Growth*, 2005, **275**, p 1269-1273

30. S.G. Oleinik and N.V. Danilenko, Primary Recrystallization Mechanism in Ceramic Materials, *Powder Metall. Met. Ceram.*, 1998, **37**(1-2), p 63-77

31. R.W. Rice, *Mechanical Properties of Ceramics and Composites: Grain and Particle Effects*, Marcel Dekker, New York, 2000, p 54-57

32. B. Gludovatz, M. Faleschini, S. Wurster, A. Hoffmann, and R. Pippan, Influence of Microstructure on the Fracture Toughness of Tungsten Alloys, *TMS Annual Meeting*, Vol 1, New Orleans, 2008, p. 449-454

33. M. Janssen, J. Zuidema, and R. Wanhill, *Fracture Mechanics*, 2nd ed., Spon Press, New York, 2009, p 285-316